

RESEARCH

Open Access



Mechanism for formation of porcine blood hydrogels used as additives in the mortar of traditional Chinese architectural painting

Cong Cheng¹, Yeting Zhu¹, Jingyi Zhang¹, Wei Li^{1,3}, Gele Teri¹, Lizhen Zheng^{2*} and Daodao Hu^{1*}

Abstract

Ancient Chinese architecture drawing is a unique form of ancient Chinese art. Porcine blood hydrogels are distinctive ingredients used to prepare the composite material of the substrate layer for architecture drawing. This investigation was focused on the mechanism for porcine blood hydrogel formation. Based on the traditional Chinese recipe for the preparation of porcine blood-lime mortar, samples with different ratios of porcine blood and lime water were prepared, and the molecular-scale interactions between the lime water and proteins in the porcine blood were examined with FTIR spectroscopy, Raman spectroscopy, XRD, XPS, fluorescence spectroscopy, contact angle and rheology studies. The mechanical properties and morphological features of the samples were detected with a rheometer, universal material testing machine and SEM. The results indicated that an appropriate amount of lime water was required for gelation of the porcine blood. With the appropriate alkalinity, sufficient carboxyl groups on the fibrin chains were deprotonated, and coordination with Ca^{2+} ions formed enough cross-links for support networks within the structure of the porcine blood hydrogel. Complexation of deprotonated carboxyl groups on the fibrin chains with Ca^{2+} ions led to the formation of a hydrophobic surface due alterations of the fibrin conformation and increased the adhesive properties of the hydrogel. With the hydrogel used as an ingredient in the preparation of a substrate layer composite, it is suggested that the hydrophobic surface of the hydrogel facilitated mixing with hydrophobic tung oil during preparation of the composite material, and strong adhesion of the hydrogel increased the mechanical strength and crack resistance of the substrate layer.

Keywords Porcine blood-lime mortar, Porcine blood hydrogel, Gelling mechanism, Lime water

Introduction

Ancient Chinese buildings are typically wooden structures and are famous for their carved beams and painted rafters. In particular, painting and colored drawings of ancient Chinese architectural heritage are highly valuable. Ancient artists used mortar as a substrate on wood to protect the lumber and prepare it for painting [1, 2]. According to the literature, the mortar applied in ancient Chinese wooden buildings consisted of a rather complex system of inorganic and organic components, including brick ash, lime, fibers, flour, porcine blood and tung oil, among which the brick ash and lime were used as filling materials, fibers were used as taut material, and flour, blood and tung oil were used as binding materials.

*Correspondence:

Lizhen Zheng
lizhenzheng@snnu.edu.cn
Daodao Hu
daodaohu@snnu.edu.cn

¹ Engineering Research Center of Historical and Cultural Heritage Protection, Ministry of Education, School of Materials Science and Engineering, Shaanxi Normal University, Xi'an 710062, China

² School of Historical Culture and Tourism, Xi'an University, Xi'an 710065, China

³ Shaanxi Engineering Research Center of Controllable Neutron Source, School of Electronic Information, Xijing University, Xi'an 710123, China



© The Author(s) 2024. **Open Access** This article is licensed under a Creative Commons Attribution 4.0 International License, which permits use, sharing, adaptation, distribution and reproduction in any medium or format, as long as you give appropriate credit to the original author(s) and the source, provide a link to the Creative Commons licence, and indicate if changes were made. The images or other third party material in this article are included in the article's Creative Commons licence, unless indicated otherwise in a credit line to the material. If material is not included in the article's Creative Commons licence and your intended use is not permitted by statutory regulation or exceeds the permitted use, you will need to obtain permission directly from the copyright holder. To view a copy of this licence, visit <http://creativecommons.org/licenses/by/4.0/>. The Creative Commons Public Domain Dedication waiver (<http://creativecommons.org/publicdomain/zero/1.0/>) applies to the data made available in this article, unless otherwise stated in a credit line to the data.

With the emergence and development of modern chemistry in the eighteenth and nineteenth centuries, the roles of various components in mortars are becoming clearer. Among these components, the porcine blood plays an important role in the mortar. In fact, the use of animal blood in mortars was mentioned in many ancient texts from both Europe and Asia [3]. As shown by archaeological discoveries, blood-lime mortar was used in Chinese architectural structures, including the Xianyang Palace Museum site, the Forbidden City, the Old Summer Palace, the Taiyuan Confucius Temple, and the walls of Yanzhou City [4–6]. It should be noted that porcine blood hydrogels were used as additives to prepare the composite substrate layers for architectural surface painting rather than as adhesives connecting building components.

Although animal blood was mixed with various materials to prepare different types of mortars for specific purposes, the primary function of the animal blood, which contains proteins, in these mortars was adhesion. Additionally, animal blood imparted unique properties to the mortars. When blood was added to mortar, it exhibited short-setting times, water resistance, strong adhesion, fireproofing, hardness and frost resistance [3, 7]. For instance, when comparing mortar samples containing blood with ordinary lime mortar samples, it was found that the capabilities of the blood-containing mortars surpassed those of regular mortars. Furthermore, the blood derived from different animals had minimal impact on the performance of these mortars, because the blood had similar functions in these mortars and the production processes [8–10]. Research on the adhesives prepared from ox blood demonstrated that wood products bonded with protein-based adhesives derived from the blood were more waterproof than those bonded with vegetable protein-based adhesives [11]. Compared with Portland cement and porcine blood-lime mortar, traditional blood mortar is better suited for restoration of cultural relics due to its compatibility and durability with the original structures [12]. Although animal glues containing proteins are adhesive materials, they are primarily used for preparing inorganic pigment pastes rather than for preparing building mortars [13].

Although several studies have been conducted on the performance and composition of porcine blood lime mortar, this mortar was prepared with a close ratio of blood to lime for direct use in masonry bonding. However, in ancient Chinese architectural paintings, porcine blood hydrogel rather than an independent mortar was used as an additive in preparation of the ground layer. According to the traditional recipe, this hydrogel was made from a mixture of porcine blood and lime water with a very low $\text{Ca}(\text{OH})_2$ -to-blood weight ratio. As

mentioned earlier, while there have been investigations on the use of porcine blood as an additive for the composite materials used as substrate layers in architectural surface painting, the scientific principles behind formation of the porcine blood hydrogels have been scarcely studied [8]. In the biological and biomedical fields, animal blood has attracted much attention in hydrogel research due to its excellent biocompatibility. In these cases, the animal blood is typically gelled via electrostatic interactions between the negatively charged proteins in blood and positively charged polymers or salts. This formation mechanism differs from that of porcine blood hydrogels used in ancient Chinese architectural surface paintings due to the different cross-linkers used. In this present research, we specifically investigated the interactions between porcine blood and lime water mixed according to traditional recipes. The aim of this research was to understand the specific molecular-scale interactions between the proteins in porcine blood and $\text{Ca}(\text{OH})_2$. We hope this work will provide useful information on this traditional material and enrich mortar technology for conservation and restoration of historic buildings.

Experiment section

Materials

Fresh porcine blood was obtained from a local suburban slaughterhouse (Xi'an, China) and sealed in buckets. It was filtered through a sieve and used as soon as possible. Calcium oxide (CaO , AR), sodium hydroxide (NaOH , AR), and calcium chloride (CaCl_2 , AR) were obtained from Sinopharm Chemical Reagent Co., Ltd. (Shanghai, China). All reagents were used directly without further purification. Deionized water (25 °C, 18.25 M Ω cm) was used to prepare the solutions.

Preparation of model samples

Preparation of lime water: Approximately 25 g of calcium oxide was added to 100 g of deionized water ($m_{\text{CaO}}:m_{\text{water}} = 0.25$). Then, lime water was kept for 24 h at room temperature. The lime water was thoroughly mixed prior to use.

Preparation of the porcine blood hydrogel: The porcine blood hydrogel was prepared according to traditional recipes. First, the PB was filtered through a 200-mesh sieve. Subsequently, 3 g of lime water was added dropwise to 100 g of porcine blood and stirred for five minutes. Finally, this mixed sample was kept at room temperature and placed for 3 h. This composite was called a porcine blood hydrogel ($\text{PBG}_{0.03}$). For comparison, model samples with different ratios of porcine blood to lime water were also prepared. The components and forms of the corresponding samples are shown in Table 1.

Table 1 Components and forms of the model samples

Samples	Blood:Lime water (g/g)	Blood:CaO (g/g)	Form
PB	100:0	100:0	Sol
PBG _{0.03}	100:3	100:0.6	Sol
PBG _{0.04}	100:4	100:0.8	Sol
PBG _{0.05}	100:5	100:1.0	Hydro-gel
PBG _{0.06}	100:6	100:1.2	Hydro-gel
PBG _{0.07}	100:7	100:1.4	Hydro-gel

* 1. PBG—a mixture of porcine blood and lime water; 2. The subscript PBG refers to the mass ratio of porcine blood to lime water

To explore the effects of alkalinity and Ca²⁺ on formation of the porcine blood hydrogels, several solutions were prepared, as shown in Table 2.

Characterization

Unless specifically stated otherwise, freeze-dried samples were used for characterization. The process for preparing the freeze-dried samples was as follows: model samples with different ratios of lime water to porcine blood were prepared and then left for 3 h. After that, the samples were quickly frozen in liquid nitrogen and then freeze-dried for 24 h.

The FTIR spectra of the model samples were recorded with a Perkin Elmer Spectrum Two FT-IR spectrometer (PerkinElmer, Waltham, MA, USA) over the wavenumber range 4000–500 cm⁻¹ with a resolution of 4 cm⁻¹. The freeze-dried sample was pulverized into a fine powder, and then KBr was mixed with the sample powder and pressed to form pellets for the FTIR analysis. To determine the secondary structure of the protein, deconvolution and second-order derivative analyses were performed with the amide I band using OMNIC 8.0 and PeakFit software [14, 15]. The protein secondary structure contents in the porcine blood after treatment with

different ratios of lime water were determined by calculating the peak areas of the secondary structures.

The Raman spectra of the freeze-dried samples were collected with a Renisha™ inVia Raman Microscope Spectrometer (Renishaw, Gloucestershire, London, Britain) with a 532 nm laser source and a resolution of 2 cm⁻¹. The powdered sample was immediately placed in the Raman spectroscopy system, and the spectrum was recorded between 200 and 2000 cm⁻¹.

X-ray diffraction (XRD) data of the freeze-dried samples were acquired with a DX-2700 X-ray diffractometer (Danyang Haoyuan Optics Instrument Co., Ltd., Dandong, China) with a Cu K α X-ray source operating at 40 kV and 30 mA.

X-ray photoelectron spectroscopy of the freeze-dried samples was performed with a Thermo Fisher ESCALAB 250Xi Spectrometer (XPS, ThermoFisher, Waltham, Massachusetts, USA), with a monochromatic Al K α X-ray source (16 kV, 15 mA), and pass energy of 100 eV for wide scans and 30 eV for high-resolution scans (lens in hybrid mode). All high-resolution scans were calibrated with the C 1 s peak at 284.8 eV as a standard [16]. High-resolution measurements were performed to determine the C 1 s, O 1 s, N 1 s, S 2p and Ca 2p binding energies. The XPS spectra were analyzed with Peak Fit software (Institute of Chemistry, Chinese Academy of Sciences, Beijing, China), which was used to determine the relative concentrations from the peak areas in units of atomic percent.

The fluorescence spectra of the freeze-dried samples were collected with an F-7000 fluorescence spectrophotometer (Shimadzu, Kyoto, Japan) with an excitation wavelength of 280 nm. The scanning range was set from 290 to 400 nm and the slit width was adjusted to 2.5 nm. The powdered freeze-dried samples were compressed into pellets with diameters of approximately 13 mm and fixed onto a solid sample holder for measurement.

The contact angles were measured with a Dataphysics OCA-20 (Dataphysics, Stuttgart, Germany). The detection process was as follows: the powdered freeze-dried

Table 2 Compositions of the samples used for exploring the roles of alkalinity and Ca²⁺ in formation of the hydrogel

Samples	Components	Status	pH
PB _{A1}	Blood:1 M NaOH=(100:15)	Viscous sol	10.37 ± 0.05
PB _{A2}	Blood:1 M NaOH=(100:20)	Strong viscos sol	10.85 ± 0.13
PB _{A3}	Blood:Saturated NaOH=(100:2)	Strong viscos sol	11.86 ± 0.63
PB _{A4}	Blood:Saturated NaOH=(100:4)	Viscous sol	13.07 ± 0.32
PB _{Ca-A2}	Blood:1 M CaCl ₂ :1 M NaOH=(100:10:20)	Viscous sol	11.10 ± 0.06
PB _{Ca-A5}	Blood:1 M CaCl ₂ :Saturated NaOH=(100:6:1)	Viscous sol	9.61 ± 0.03
PB _{Ca-A6}	Blood:1 M CaCl ₂ :Saturated NaOH=(100:6:2)	Strong viscos sol	11.74 ± 0.22
PB _{Ca-A7}	Blood:1 M CaCl ₂ :Saturated NaOH=(100:6:3)	Hydrogel	12.95 ± 0.03

sample was pressed onto double-sided adhesive tape fixed on a glass slide, and then the water droplet was dropped on the surface of the sample and left for 10 s and 60 s to measure the contact angle. Three different points on each sample were selected for testing, and the average value of the three determinations was obtained.

Model samples with varying ratios of lime water to porcine blood were prepared as described above, and their viscosities were measured with a TA Instruments AR-G2 rheometer (TA Instruments, Milford, Massachusetts, U.S.) at a shear rate range of 0.001–20 s⁻¹. These measurements were conducted with a rotor suitable for low-viscosity liquids at a constant temperature of 23 °C.

The freeze-dried samples were mechanically broken, and their cross-sectional morphologies were observed with an SU-3500 scanning electron microscope (SEM, Hitachi, Tokyo, Japan) at an accelerating voltage of 5 kV. The model samples were sprayed with gold before measurement.

To investigate the roles of proteins in gelling of the porcine blood, intermolecular forces in the blood hydrogel were detected with the method described by Perez-Mateos et al. [17–19] with appropriate modifications. The blood hydrogel was successively solubilized in four solutions, 0.8 M sodium chloride (S1), 4 M urea + 0.8 M sodium chloride (S2), 8 M urea + 0.6 M sodium chloride (S3), and 0.5 M β-mercaptoethanol + 0.8 M sodium chloride + 4 M urea (S4), and the protein solubilities in the solutions were determined after the treatments. The typical process was as follows. Approximately 5 g of PBG_{0.05} was added to 10 mL of S1 solution, placed in a sonicator for 3 min, and then placed in a low-temperature refrigerator (operating temperature 5–8 °C) for 1 h. The resulting homogenate was centrifuged at 10,000 r/min for 10 min (GL-20G-II centrifuge, Shanghai Anting Scientific Instrument Factory, Shanghai, China). The supernatant was kept in a low-temperature refrigerator. The same volume of trichloroacetic acid solution with a concentration of 20% was added to the supernatant and centrifuged at a speed of 10,000 r/min for 10 min. Then, the obtained precipitate was dissolved in 1 mL of 1 M NaOH. The protein concentration of the solution was obtained with the biuret test. The precipitate obtained from S1 was homogenized in 10 mL of S2 and then subjected to the same process described above and then again with 10 mL of S3 and finally with 10 mL of S4. The same procedures were also performed with S3 and S4. The protein concentrations in the supernatants were detected as described above. In the aforementioned processes, the precipitates formed after treatment with different solutions were attributed to varying chemical bonds between the proteins in the porcine blood hydrogel. The percentage of

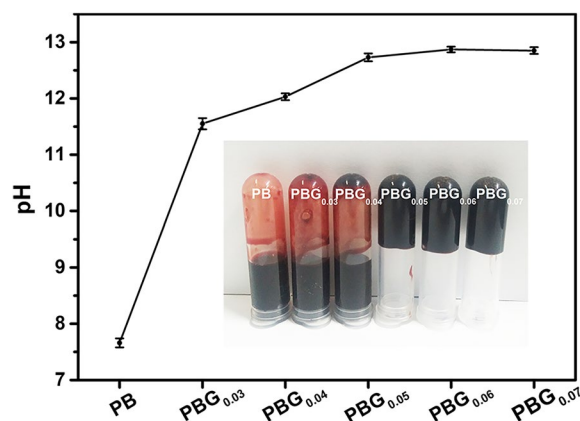


Fig. 1 Effect of the ratio of porcine blood to lime water on the pH and the status of the mixture. The insert shows photos of the corresponding samples after 3 h of mixing the porcine blood and lime water

soluble protein in each fraction was expressed as a proportion of the total protein.

The bonding shearing strength of the model samples was tested at room temperature with a universal material testing machine (Minks Testing Equipment Co., Ltd., Xi'an, China). ISO standard method 6237:2017 was followed to determine the bonding shearing strength. Two wooden strips were bonded to the model samples in a 2.5 × 2 cm adhesive area (Additional file 1: Figure S1), and the bonded samples were clamped at room temperature for 24 h to dry. The dried samples were stretched at a crosshead speed of 5.0 mm/min, and the maximum shearing strength was recorded. The measured result for each sample was the average from seven determinations.

Results and discussion

Effect of alkali and calcium ions on hydrogel formation with porcine blood

The role of the porcine blood hydrogels used in ancient Chinese architectural paintings differed from that of porcine blood lime mortar used in masonry bonding. Porcine blood lime mortar was primarily utilized for bonding, with a close ratio of porcine blood to lime slurry. Porcine blood hydrogels, which were prepared with a lower ratio of lime water to porcine blood, were mainly employed to improve the mechanical properties of the tung oil used in ancient architectural paintings. Based on the components of the model samples presented in Table 1, Fig. 1 shows the effect of lime water on the formation of porcine blood hydrogels. These results indicate that the formation process required a sufficiently high pH and an adequate concentration of Ca²⁺. Due to difficulties in dispersing porcine blood effectively in tung

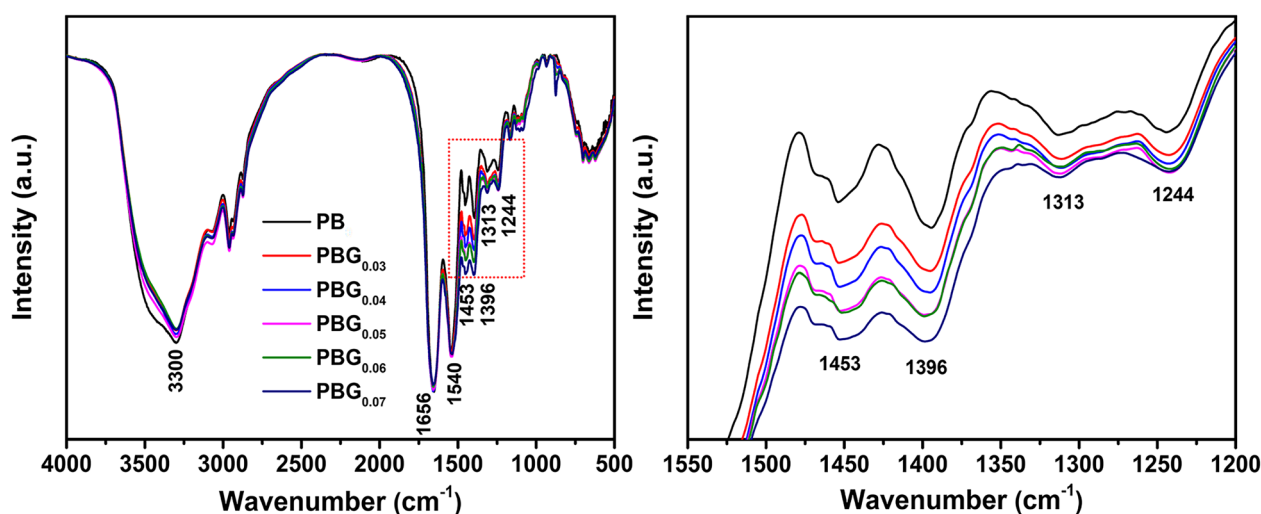


Fig. 2 FTIR spectra of the model samples prepared with different ratios of porcine blood to lime water (left) and partial enlargements (right)

oil, it is anticipated that this soft hydrogel was stirred and cut into small pieces to facilitate dispersion.

To investigate the roles of the alkali and Ca^{2+} in formation of the porcine blood hydrogels, samples of porcine blood mixed with solutions of NaOH and different concentrations of Ca^{2+} were prepared as shown in Table 2. The formation of porcine blood hydrogels required an appropriate pH and calcium ion concentration [20, 21]. The results obtained from this set of experiments were consistent with those obtained in Fig. 1. This is why an appropriate amount of limestone was necessary for the formation of porcine blood hydrogels, as it ensured that both the proper pH level and calcium concentration were provided simultaneously. The corresponding mechanisms will be discussed below.

Table 3 Assignments of the main spectral bands in the infrared spectra of proteins [23, 24]

Position (cm^{-1})	Assignment
3400	N–H stretching
3300	O–H stretching
1656	Amide I (C=O stretching)
1540	Amide II (protein N–H bending, C–N stretching)
1453	C–H deformation vibration
1396	COO ⁻ stretching
1313	CH ₂ deformation
1244	CH ₂ deformation
1169	Side chain

FTIR spectra of the porcine blood hydrogels

Figure 2 shows the FTIR spectra of the model samples. The main peaks observed in their FTIR spectra were the amide I bands ($1700\text{--}1600\text{ cm}^{-1}$), amide II bands ($1575\text{--}1480\text{ cm}^{-1}$) and amide III bands ($1265\text{--}1230\text{ cm}^{-1}$) of the proteins [22]. The assignments for these peaks are provided in Table 3. The intensities of the peaks at 3400 cm^{-1} , 1453 cm^{-1} , 1395 cm^{-1} , 1313 cm^{-1} and 1244 cm^{-1} , obviously changed with changes in the ratio of porcine blood to lime water (Fig. 2 (left and right)). As more lime water was added to the porcine blood, the increased alkalinity decreased the intensity of the peak centered at 3400 cm^{-1} due to changes in both the N–H stretching vibrations of the proteins and the H–O–H stretching vibrations of the water molecules [23]. Additionally, there was an increase in the peak located at 1395 cm^{-1} , which was attributed to the symmetric stretching vibrations of COO⁻ groups resulting from deprotonation of the carboxyl groups in the protein side chains [6, 8, 23, 24]. The change in the peak at 1453 cm^{-1} was due to CH₃ and CH₂ bending vibrations within protein side chains [23]. Furthermore, the changes in the peaks at 1313 cm^{-1} and 1244 cm^{-1} were derived from out-of-plane rocking vibrations of long-chain –CH₂– groups. These changes indicated exposed conformations of the protein side chains caused by the lime water [25]. The alkalinity led to conformational changes in the proteins as well as deprotonation of the acidic amino acids to form cross-linking bonds between Ca^{2+} ions and deprotonated carboxyl groups. Therefore, for hydrogels to form within porcine blood, a greater proportion of lime water was required [26]. The aforementioned changes

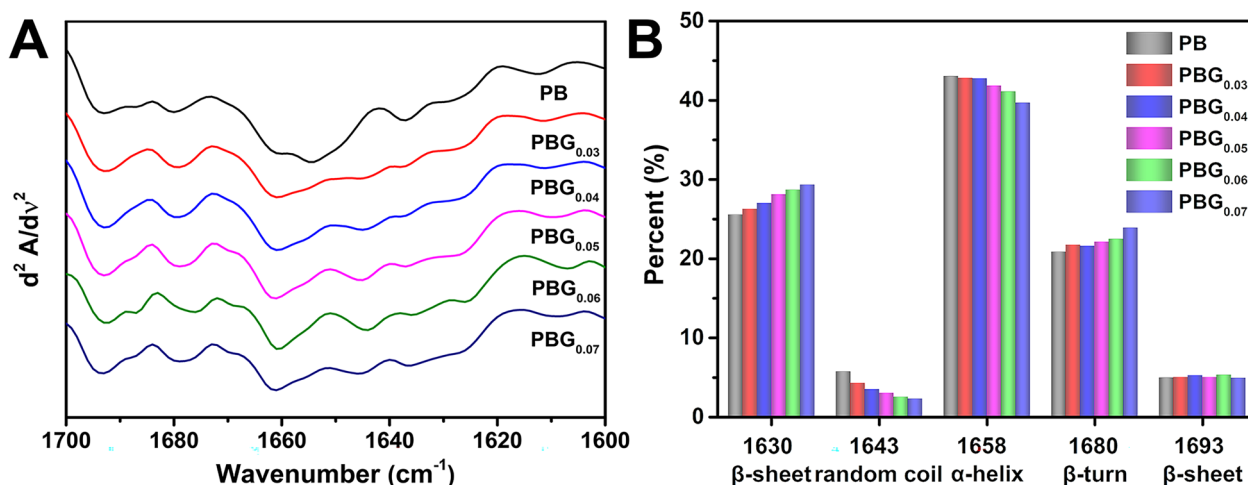


Fig. 3 Second derivative FTIR spectra of the amide I region of model samples prepared with different ratios of porcine blood to lime water (A) and the proportions of protein secondary structures in the corresponding samples (B)

observed in the peaks were consistent with the trend for porcine blood hydrogel formation shown in Fig. 1.

Features of the secondary structures of proteins in the porcine blood hydrogels

The peak positions of the amide I C=O bands (1656 cm^{-1}) in the spectra of the porcine blood and the model samples were similar, as shown in Fig. 2. Generally, the sensitive stretching vibrations of the C=O groups in the amide I bands of the protein backbone are associated with the secondary structures, each of which corresponds to a different C=O stretching frequency. In other words, changes in the intensity of the amide I band primarily reflect movements in the polypeptide backbone [23]. Therefore, the variations of the amide I band can be used to assess the conformational changes in proteins [15]. The main secondary structures include α -helices, β -turns, random coils, and β -sheets. Figure 3A displays the second derivative FTIR spectra from Fig. 2 within the range $1700\text{--}1600\text{ cm}^{-1}$.

The fitted curves for the characteristic peaks of the protein secondary structures in the amide I bands ($1700\text{--}1600\text{ cm}^{-1}$) for the different model samples are shown in Fig. 4, based on the results of the second derivatives. According to previous studies [27, 28], β -sheets (intermolecular aggregates), random coils, α -helices, β -turns and β -sheets (intramolecular aggregates) gave rise to peaks at 1630 cm^{-1} , 1643 cm^{-1} , 1658 cm^{-1} , 1680 cm^{-1} and 1693 cm^{-1} , respectively.

Our results showed that the proteins in the porcine blood were dominated by α -helices. After treatment with the lime water, the proportions of α -helices (1658 cm^{-1}) and random coils (1643 cm^{-1}) decreased,

the proportions of β -sheets (1630 cm^{-1} intermolecular) and β -turns (1680 cm^{-1}) increased, and the proportions of β -sheets (intramolecular aggregates at 1693 cm^{-1}) did not change significantly. Increased amounts of lime in porcine blood made the changes in the secondary structure more apparent. These findings were consistent with those of Zhao [20], who showed that the proteins in porcine blood predominantly exhibited α -helices. Under the influence of lime water, the proportions of α -helices (1658 cm^{-1}) and random coils (1643 cm^{-1}) decreased, while those of β -sheets (1630 cm^{-1} intermolecular) and β -turns (1680 cm^{-1}) increased. However, there was no significant change in β -sheets (intramolecular aggregates) at 1693 cm^{-1} . Increasing the concentration of lime in porcine blood made these changes in secondary structure more pronounced. Additionally, these changes in the protein secondary structures induced by lime water were consistent with other reports in the literature. Lime water disrupted the internal hydrogen bonds of proteins, leading to unfolding of the α -helices and the formation of β -sheets (intermolecular aggregates). This resulted in a decrease α -helix content and an increase β -sheets content, which increased the number of hydrophobic groups on the surface of the molecule. These hydrophobic groups interacted with each other and formed aggregates, and the resulting hydrogel reduced the water mobility [23, 29]. FTIR spectra and changes in the protein secondary structures revealed molecular-level structural changes in porcine blood treated with different ratios of lime water, providing further understanding of the process by which hydrogels are formed when porcine blood is treating with lime water.

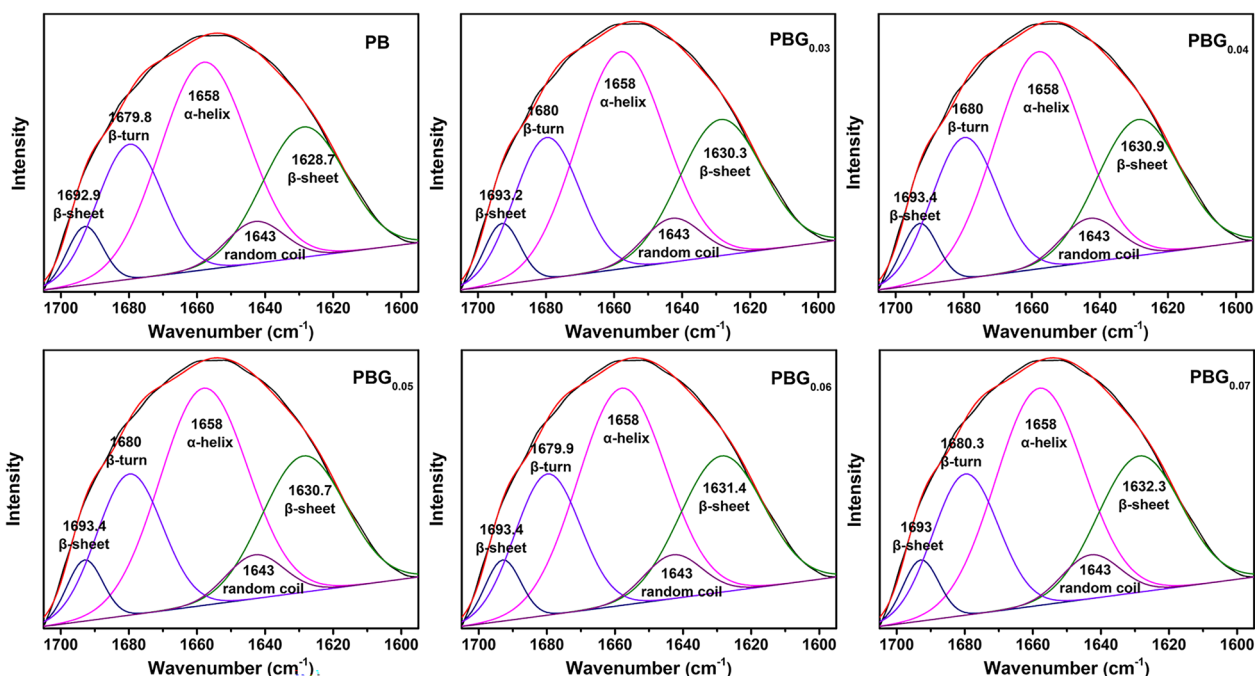


Fig. 4 Fitted curves for the characteristic peaks of the protein secondary structures in the amide I region (1600–1700 cm^{-1}) of the model samples prepared in different ratios of porcine blood to lime water

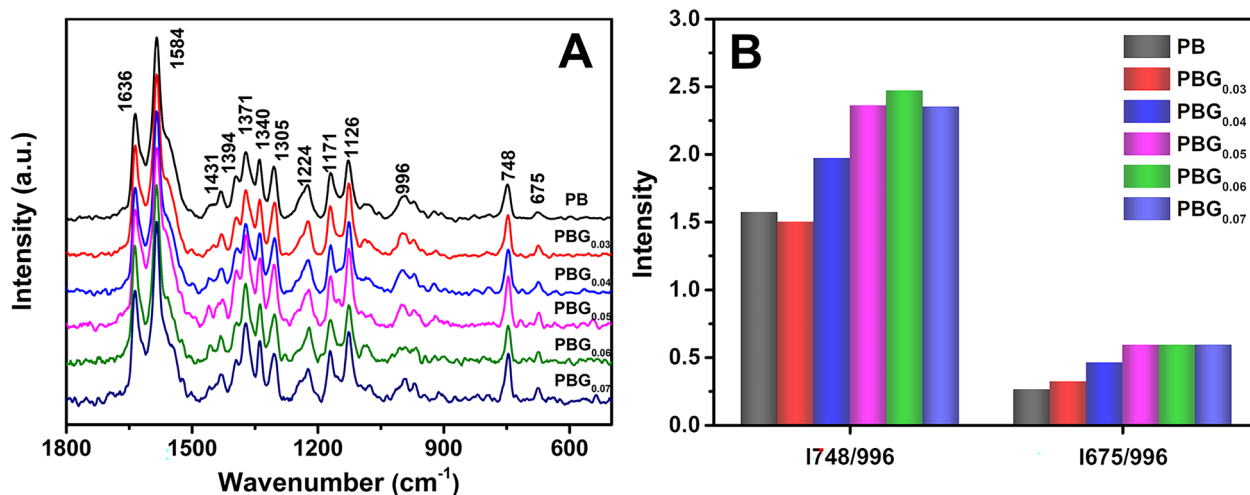


Fig. 5 **A** Raman spectra of model samples prepared with different ratios of porcine blood to lime water and **B** the corresponding $I_{748/996}$ and $I_{675/996}$ ratios

Raman spectra of the porcine blood hydrogels

The Raman spectra of the model samples are shown in Fig. 5A. Table 4 lists the Raman peaks for the functional groups in the protein based on the literature on whole blood and proteins [30, 31]. The band at 1636 cm^{-1} was identified as the protein amide I band, which was related to the protein backbone structure. The band at 1224 cm^{-1} was the amide III band, which involved the

C–N stretching vibrations and N–H plane bending vibrations of peptide bonds, as well as the C–C stretching vibrations and C=O plane bending vibrations of peptide bonds [32]. Although these peaks can be used to determine the protein secondary structures, the dense spectral peaks near them provide significant interference, which limits their use in secondary structural studies of certain proteins. In fact, the changes in some peaks originating

Table 4 Peak positions and assignments of the Raman spectra for the proteins with 532 nm laser irradiation [33, 36]

Peak Position (cm ⁻¹)	Structure feature	Region/assignment
1636	α-helix	Amide I (C=O stretch)
1584	Heme	vibrations of phenylalanine, C=C stretch, G A,
1431	/	CH ₂ /CH ₃ amino acid deformation
1371	Lipids	CH ₃ symmetric stretch
1340	/	C–H deformation
1305	α-helix	Amide III α-helix/CH deformation
1224	β-sheet/Protein	Amide III/C _α –N stretch, N–H deformation
1171	Tyr	deformation vibrations of CC group, Tyr (C–H inplane)
1126	Glucose	deformation vibrations of C–N group
996	Phe	vibrations of phenylalanine, aromatic ring breathing
748	Trp	tryptophan vibration
675	Cys	Cys (C–S stretch)

from amino acid residues are often utilized for protein secondary structure analyses. The conformation of the side chain is detectable within the range 500–1000 cm⁻¹, and the peaks in this range are attributed to individual amino acid residues. The peaks for the aromatic amino acid side chains can be used to determine the polarity of the microenvironment. The intensity of the peak for phenylalanine at 996 cm⁻¹ remains constant regardless of the protein structure and serves as an internal standard for Raman spectroscopy [26]. The I_{748/996} intensity can be used to measure the hydrophobicities of tryptophan residues and reflect the hydrophobic interactions of the protein hydrogel. The I_{675/996} intensity was also used in hydrophobic environments [33–35]. Based on the Raman spectra shown in Fig. 5A, the I_{748/996} and I_{675/996} ratios of the model samples prepared with different ratios of porcine blood to lime water were calculated. The results are shown in Fig. 5B. Both the I_{748/996} and I_{675/996} ratios increased with increasing lime water content in the model samples, indicating changes in the protein conformations due to the presence of lime water, which exposed tryptophan and cysteine from their original encapsulated hydrophobic environments. This conclusion was consistent with that obtained with the infrared spectroscopy.

XRD patterns of the porcine blood hydrogels

The XRD patterns of the model samples were determined to explore the crystal structures of the components. The results are shown in Fig. 6A. For the PB sample, there were only two broad diffraction peaks at 2θ values of approximately 9.4° and 20.5°, for the α-helix and β-sheet structures, respectively, of the protein molecules [37]. In the PBG model sample (a mixture of porcine blood and lime water), the intensities of these two diffuse diffraction peaks decreased with increasing lime water content, indicating that lime water decreased the short-range

order of the proteins in the porcine blood [38, 39]. With increases in the lime water, the position of the diffraction peak shifted slightly to lower angles. The decreased height and broadening of the peak suggested a loss of short-range ordered domains and an expansion of the lattice [37, 40, 41]. This conclusion was consistent with the changes observed in the local secondary structure contents obtained from the FTIR and Raman spectra mentioned above. Additionally, for the PBG_{0.05}, PBG_{0.06}, and PBG_{0.07} samples, sharp diffraction peaks appeared at 18°, 28.8°, and 34°, which corresponded to the (001), (100), and (101) planes of Ca(OH)₂, respectively (PDF card no. 84–1270). These peaks were increased by the lime water. For PBG_{0.03} and PBG_{0.04}, these peaks almost disappeared, which was attributed to the excess lime water cross-linked with the porcine blood proteins so that there was no excess Ca(OH)₂ in the hydrogel.

These results indicated that lime water caused gel-ling of the porcine blood, leading to changes in the protein aggregates in the porcine blood. Furthermore, this effect was more pronounced with increasing in lime water concentrations. These findings were consistent with the conclusions drawn from the spectroscopic studies. Additionally, these results suggested that excess Ca(OH)₂ resulted in the formation of a Ca(OH)₂ phase. It is thought that the excess calcium hydroxide in the porcine blood hydrogel reacted with the carbon dioxide in the air to generate CaCO₃, which would serve as a filler to increase the mechanical strength of the dried porcine blood hydrogel.

XPS spectra of the porcine blood hydrogels

XPS spectroscopy provided further evidence of changes in the molecular structure of the porcine blood hydrogel. Wide-scan and high-resolution XPS spectra, including C 1 s, N 1 s, O 1 s, S 2p, and Ca 2p spectra, were

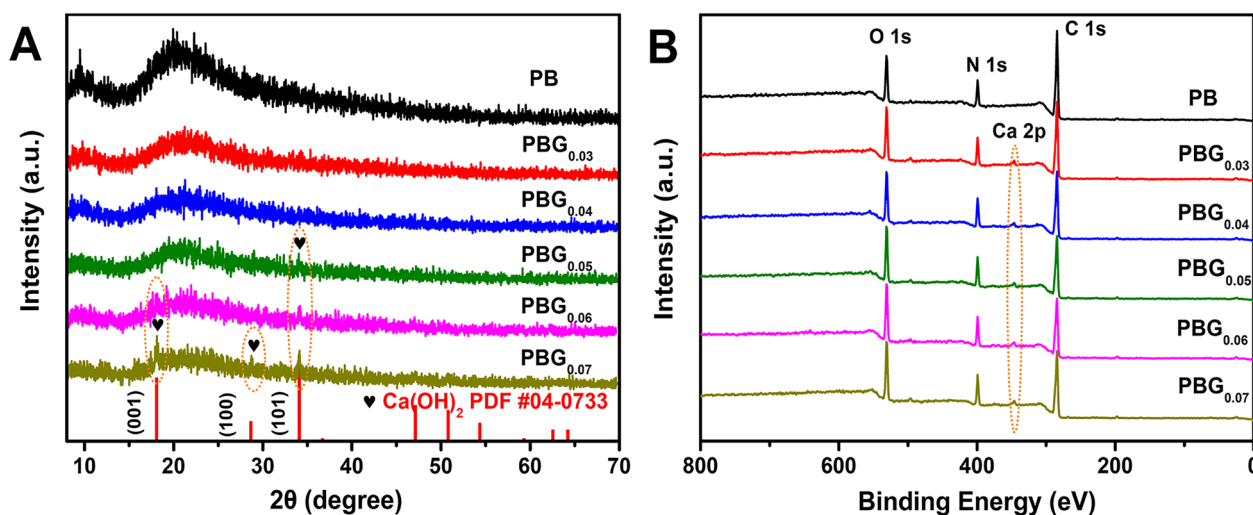


Fig. 6 **A** XRD patterns and **B** XPS wide-scan spectra of model samples prepared with different ratios of porcine blood to lime water

collected from all samples. The wide-scan XPS spectra are shown in Fig. 6B. Table 5 lists the atomic compositions determined by XPS for all samples. The peaks observed at approximately 284 eV, 531 eV, and 400 eV for all samples indicated that C, O, and N were the major elemental constituents in the model samples. As shown in Fig. 6B, a new peak at ~ 346 eV for the Ca^{2+} binding energy appeared in all model samples except for the PB sample due to the addition of lime water to porcine blood to initiate the reactions between Ca^{2+} and amino acid residues.

To explore the interactions between lime water and porcine blood, deconvoluted high-resolution XPS spectra were generated, and the results are presented in Fig. 7. The calculated data for the atomic compositions of the model samples prepared with different ratios of porcine blood to lime water and O/C and N/C ratios are shown in Table 5. The data in Table 5 revealed the following features: in comparison to those in PB, the C contents in the model samples were lower, while the contents of O, S and Ca were higher. The former was related to the

conformational changes of the proteins in porcine blood induced by the lime water, and the latter was associated with increased quantities of lime water added to porcine blood.

The deconvoluted spectra in Fig. 7 show the distribution of functional groups related to a given element. For all samples, the C 1s spectrum showed three representative structural domains with binding energies of 284.8 eV, 286 eV, and 288 eV, and these were, attributed to C1 ($\text{C}-\text{C}$, $\text{C}-\text{H}$), C2 ($\text{C}-\text{OH}$, $\text{C}-\text{N}$, $\text{C}-\text{S}$) and C3 ($\text{O}=\text{C}-\text{N}$, $-\text{C}-\text{OH}$, $-\text{COO}^-$), respectively [42, 43]. The quantitative results for these three groups containing C atoms are shown in Table 6. Compared with those of the PB samples, the contents of C1 and C3 increased, while the content of C2 decreased. These changes were closely associated with changes in the distribution of amino acid residues in the fibrin chains. The fibrin chains contained several amino acid functional groups, including $-\text{COOH}$ (from glutamic acid (9%) and aspartic acid (10%)), $-\text{C}-\text{OH}$ (from serine acid (21%) and threonine acid (11%)), pyrrolidine (from proline (12%)), and $-\text{CH}_2$ (from glycine

Table 5 Atomic compositions of the model samples prepared with different ratios of porcine blood to lime water

Samples	Atomic content (%)					O/C	N/C
	C 1s	N 1s	O 1s	Ca 2p	S 2p		
PB	49.01	23.87	26.84	0.00	0.29	0.55	0.49
PBG _{0.03}	43.07	26.24	27.43	2.54	0.71	0.64	0.61
PBG _{0.04}	41.79	26.13	28.90	2.72	0.46	0.69	0.63
PBG _{0.05}	41.35	24.85	30.42	2.81	0.56	0.74	0.60
PBG _{0.06}	40.00	22.80	33.72	2.91	0.57	0.84	0.57
PBG _{0.07}	42.02	22.30	32.18	2.94	0.57	0.77	0.53

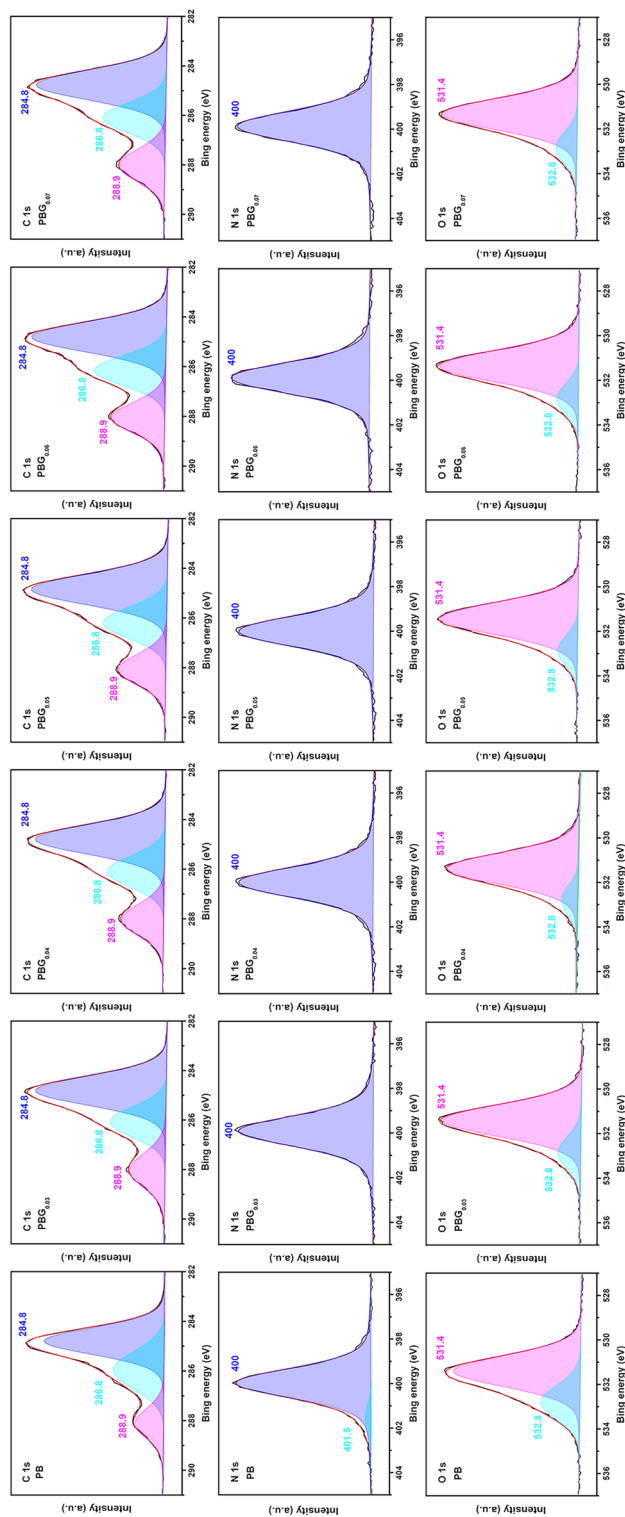


Fig. 7 Deconvoluted high-resolution C 1s, N 1s and O 1s XPS spectra for model samples prepared with different ratios of porcine blood to lime water

(18%) [44]. Exposure of the conformational surface to segments rich in glutamic acid, aspartic acid and glycine [45] increased the proportions of C1 and C3. However, the segments rich in proline, serine acid, and threonine acid embedded inside the domains of the fibrins led to a decrease in C2. The main driving force for the conformational changes was the coordination of Ca^{2+} to the carboxyl groups on the fibrin chains [45]. This effect drove the changes in the aforementioned segments.

Deconvolution of the high-resolution O 1 s XPS spectrum indicated two main species, O1 ($-\text{COO}^-$, 531.4 eV) and O2 ($-\text{OH}$, 532.8 eV) [46]. The increased proportion of O1 and decreased proportion of O2 with lime water addition were consistent with the changes in C2 and C3 mentioned above. The N1s spectra were divided into two peaks at approximately 399.9 eV and 401.4 eV, corresponding to amine/amide ($\text{N}-\text{H}$, $\text{O}=\text{C}-\text{N}$) and protonated amine ($-\text{NH}_2^+$) [43], which were most likely derived from the aforementioned protein chain backbones and segments rich in proline. The decreased $-\text{NH}_2^+$ content with increasing lime water content was attributed to deprotonation of proline by lime water.

The high-resolution Ca 2p and S 2p XPS spectra are shown in Fig. 8. Deconvolution of the S 2p spectrum revealed three peaks at 159.5 eV and 164.1 eV, which were assigned to the S 2p_{3/2} and S 2p_{1/2} states [47–49], respectively, and SH and S–S groups. This was consistent with the thiol residues from cysteine and disulfide bonds in fibrin [44, 50]. The peak at 168.8 eV for the model sample treated with lime water was attributed to S–O species (sulfate or sulfite), which arose from heme-dependent catalytic sulfide oxidation of porcine blood [51]. However, for the PB sample, this peak was not present in the deconvoluted high-resolution S 2p spectrum because the sulfhydryl groups were buried in the hydrophobic nuclear center inside the molecule [52]. These results suggested that lime water exposed the sulfhydryl groups located inside the fibrin proteins to the surface, which enabled oxidation to disulfide bonds. The conclusion drawn from the high-resolution XPS spectra were consistent with previous findings that lime water induced conformational changes in the fibrin proteins.

The high-resolution Ca 2p spectra of the model samples treated with lime water revealed two peaks with binding energies of 347.1 eV and 350.6 eV for the Ca 2p_{1/2} and Ca 2p_{3/2} states, respectively. The difference between the two peaks was approximately 3.5 eV, indicating that calcium had a valence of +2 [53, 54].

Based on the aforementioned discussion, the following conclusions were drawn. In the porcine blood hydrogels, the cross-linking bonds involved coordination between calcium ions and carboxyl groups from the glutamic acid and aspartic acid residues. Additionally, catalytic

oxidation was evident in the porcine blood hydrogels, which was attributed to the presence of heme [55].

Hydrophobicity of the porcine blood hydrogels

The endogenous fluorescence of proteins is mainly derived from tryptophan and tyrosine, which are aromatic amino acid residues. Tryptophan residues are sensitive to changes in the microenvironment and are utilized as fluorescent probes in studying protein conformations [39, 56]. The fluorescence spectra resulting from excitation of the model samples at 280 nm are shown in Fig. 9A. The emission peaks at approximately 320 nm for all samples indicated that these emissions arose from tryptophan residues in the protein [57]. The spectra also demonstrated that the intensity of the maximum emission peak gradually increased with increasing lime water content, and the maximum emission wavelength shifted from 319 to 324 nm. These changes were associated with alterations in the microenvironments of the tryptophan residues resulting from conformational changes in the fibrin. It was concluded that tryptophan located in a polar environment exhibits a redshifted fluorescence peak [20, 58], while increased emission intensity resulted from an increase in the number of exposed fluorescent tryptophan residues on the surface of the protein [59]. Our results are consistent with literature reports suggesting that higher pHs lead to slight redshifts and slightly higher emission intensities for the tryptophan residues in the fibrin, indicating a structural transition toward an unfolded conformation induced by pH changes [60].

Due to the different protein conformation, the tryptophan initially wrapped in a nonpolar environment was exposed. Consequently, the hydrophobicity amino acid residues around tryptophan were also exposed [61]. Specifically, the higher pH created a new hydrophobic environment within the folding-unfolding system [60]. Our findings were consistent with previous literature reports of increased surface hydrophobicity and changes in the protein secondary structures after protein gelatinization.

The contact angles of the model samples measured at different times are shown in Fig. 9B. The water droplets were held on each sample for 10 s and 60 s, respectively. The results indicated that the hydrophobicities of the model samples increased with increasing lime water contents. Undenatured proteins typically have spherical particle shapes, with most hydrophobic side chains buried inside the globular proteins to form a dense, spherical structure [62]. For the fibrin protein in porcine blood, increases in the pH cause denaturation and expose some hydrophobic groups within the conformational structure [11, 60]. In fact, the hydrophobic nature of the dried porcine blood hydrogel is required for its use as a protective coating material; in manufacturing the substrate layers

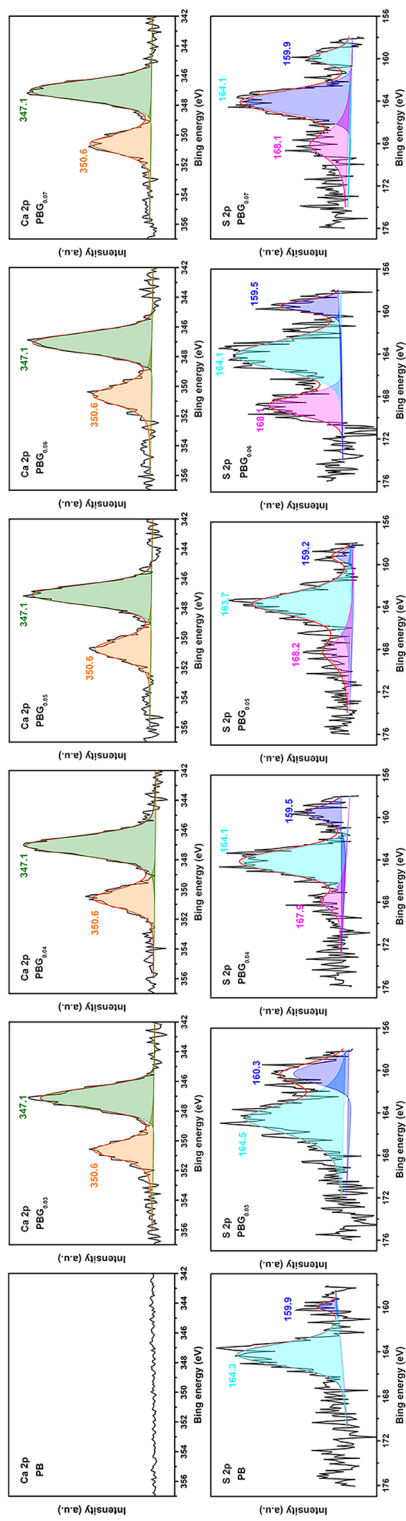


Fig. 8 Ca 2p and S 2p high-resolution XPS spectra for model samples prepared with different ratios of porcine blood to lime water

for Chinese architectural paintings, this hydrophobicity also increases the compatibility between the porcine blood hydrogel and tung oil.

Changes in the rheological properties of the porcine blood hydrogels

The rheological behavior of a solution reflects complex intermolecular interactions [63, 64]. By measuring the rheologies of the model samples, we obtained information on the interactions between the lime water and fibrin proteins. Figure 10A shows the viscosity curves for model samples with different ratios of porcine blood to lime water after mixing for 17 min. Compared to those of the PB sample, the curves for PBG_x exhibited typical shear-thinning. This shear-thinning provided dispersion of the porcine blood hydrogels for in preparing the composite materials.

Shear thinning refers to decreased viscosity as the shear rate increases, indicating a transition from an entangled intermolecular structure to a disentangled one [10, 65]. Fibrin protein chains contain abundant amino acid residues with carboxyl groups [44]. In the mixtures of lime water and porcine blood, these carboxyl groups coordinate with Ca²⁺ to form cross-linked structures [29], which are broken by shearing action, resulting in decreased viscosity. The increased viscosity seen with more lime water was attributed to increased cross-linking due to coordination between calcium ions and carboxyl groups on the fibrin protein chains. This intermolecular interaction enhanced the adhesion strength of the porcine blood hydrogels.

The rheology of the porcine blood gelled by lime water was determined to reveal its kinetic characteristics. The rheologies of the porcine blood hydrogels were examined at different times after mixing with lime water at a ratio of 0.05, and the results are shown in Fig. 10B. Herein, the model sample PBG_{0.05}, which closely resembled the traditional recipe, was chosen as a typical sample. Obviously, the viscosity increased with increasing standing time for the porcine blood mixed with lime water, suggesting that a network of fibrin cross-linked with calcium ions formed after a certain delay, which was associated with slow diffusion of the cross-linking agents and the entangled conformation of fibrin [66]. First, blood with a certain viscosity hindered the diffusion of lime water to some extent. Second, transformation of the protein aggregated morphology and the creation of cross-linked structures involved specific processes. The alkali acted on fibrin, deprotonated the acidic amino acid residues and formed carboxyl groups. Furthermore, the calcium ions bonded with these carboxyl groups, achieving chemical cross-linking of protein molecules. The aggregated blood fibers were disaggregated by electrostatic repulsion

between the protein chains due to alkali. During hydrogelation, the calcium ions formed coordination bonds with the negatively charged carboxyl groups to form chemical crosslinked structures [29].

Micromorphologies of the porcine blood hydrogels

Model samples with different ratios of porcine blood to lime water were prepared, as shown in Table 1, and the statuses of the model samples are illustrated in Fig. 1. Freeze-drying is often used to maintain the network structures of swollen hydrogels during the drying process. Therefore, this method was used to observe the evolutions in the porous morphology of the swollen model samples with changes in the ratio of blood to lime water. First, all fresh model samples were cryogenically hardened by quenching them in liquid nitrogen and then freeze-dried under vacuum with a freeze dryer. The freeze-dried model samples were examined with SEM to study their cross-sections, and the results are shown in Fig. 11A. All samples exhibited porous structures, with gray regions indicating protein accumulation and black areas representing water depletion [67]. These porous structures indicated the formation of network structures through protein interactions. According to Guo [68], hydrogels are colloidal phases in which numerous hydrogels fix the flow of solvent molecules by forming a three-dimensional network composed of fiber columnar structures. Figure 11A also shows that introduction of varying amounts of lime water into the porcine blood resulted in noticeable differences in the microstructural morphologies. Samples with less lime water, such as PB, PBG_{0.03} and PBG_{0.04}, exhibited lamellar pore structures that gradually weakened with increasing amounts of lime water added. Further addition of lime water (e.g., samples PB_{0.05}, PBG_{0.06} and PBG_{0.07}) led to homogeneous

Table 6 Proportion (at. %) of carbon in different chemical environments, as detected by XPS for the model samples prepared with different ratios of porcine blood to lime water

Samples	C1 (284.8 eV) (C–C, C–H)	C2 (286 eV) (C–OH, C–N, C–S)	C3 (288 eV) (O=C–N, –C(=O)–OH, O=C–O [–])
PB	53.80	30.76	15.44
PBG _{0.03}	56.71	24.34	18.94
PBG _{0.04}	55.94	24.80	19.26
PBG _{0.05}	54.80	25.56	19.64
PBG _{0.06}	51.87	26.83	21.30
PBG _{0.07}	53.85	25.81	20.34

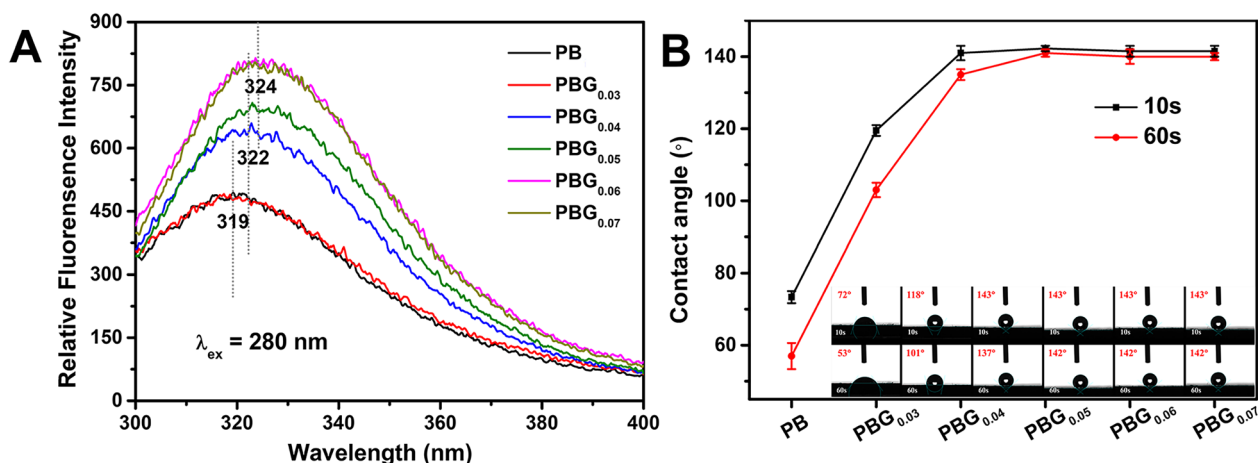


Fig. 9 **A** Fluorescence spectra ($\lambda_{ex}=280\text{ nm}$) and **B** water contact angles of model samples prepared with different ratios of porcine blood to lime water

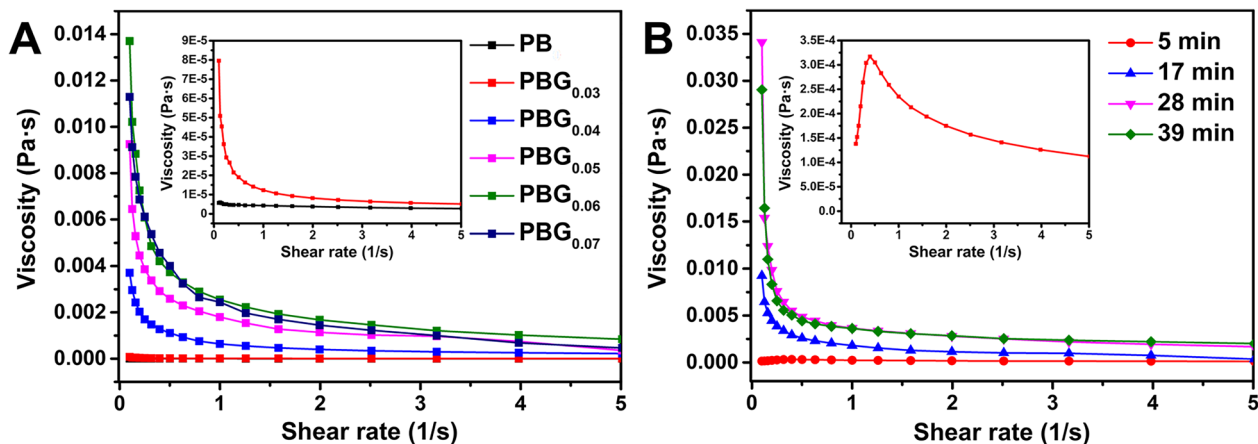


Fig. 10 **A** Viscosity curves for model samples prepared with different ratios of porcine blood mixed with lime water for 17 min; **B** Viscosity curves for mixtures of with given ratios of porcine blood to lime water ($PBG_{0.05}$) and different reaction times

pore distributions and higher pore densities. Clearly, the amount of lime water had a significant impact on the protein aggregation micromorphology due to conformational changes in the fibrin caused by alkali and Ca^{2+} .

Fibrin, the main structural protein in blood clots [69], is composed of bundles of protofibrils consisting of two half-staggered strands of fibrin monomers. Protofibrils can bind together longitudinally through knob-hole interactions to form dimers and trimers or larger oligomers, which then aggregate laterally to form double-chained aggregates with bilateral junctions [70, 71]. Elongation and thickening of the fibrin fibers are accompanied by branching due to their self-assembled structures, which is necessary for producing a three-dimensional network [71]. The freeze-dried porcine blood, as shown in Fig. 12A (PB), exhibited a furcate lamellar structure as expected. The pH and ionic strength influenced the fibrin

assembly and affected the network structure [69]. Hydrogel formation was inhibited below pH 5.3 and above 10 due to electrostatic repulsions between fibrinogen molecules with end-to-end alignments [72]. Fibrin proteins, with pI values of 5.8, are relatively rich in basic and acidic amino acid residues [44]. At lower or higher pH values, protonation or deprotonation of these residues occurs, leading to positive or negative charges on the protofibrils. In both cases, the assembled fibrin disaggregated due to electrostatic repulsion [20, 73], which inhibited porcine blood gelation. However, the appropriate pH facilitated hydrogen bonding between fibrins molecules, which increased the viscosity of the porcine blood. The amount of NaOH needed to change the viscosity changed the porcine blood, as shown in Table 1. To illustrate the effect of alkalinity on fibrinolysis, SEM images were recorded for the freeze-dried porcine blood after adjusting its pH

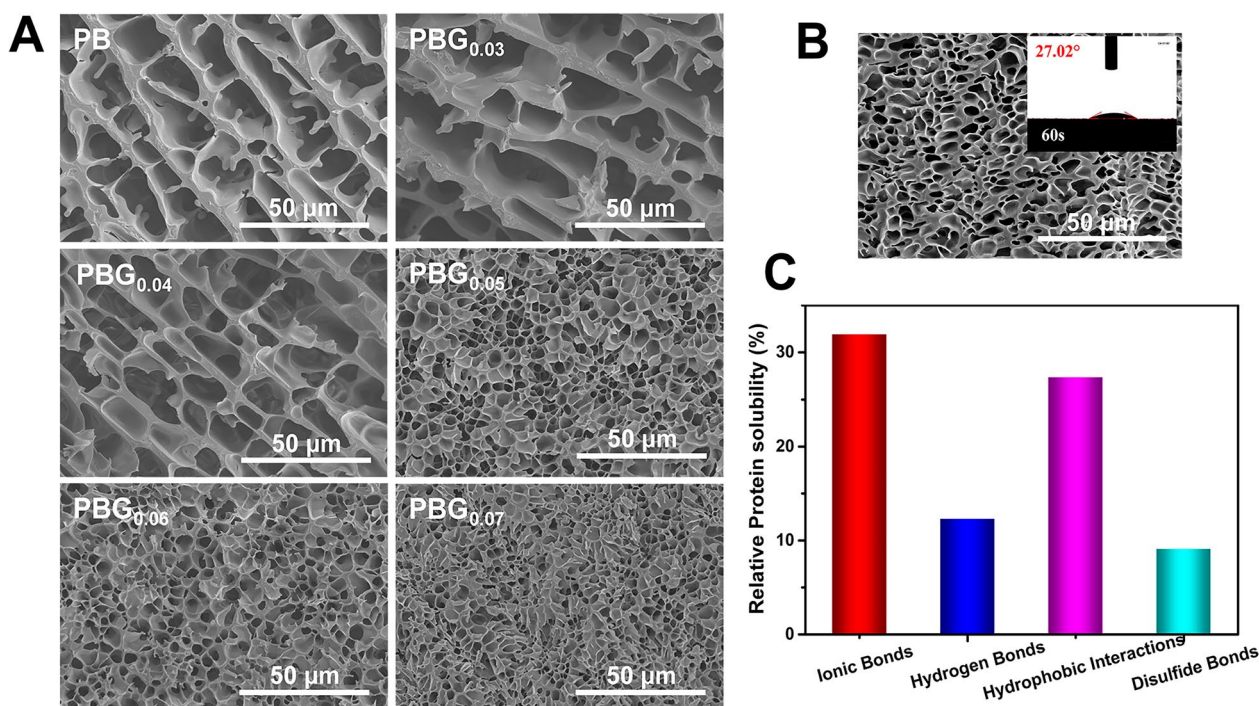


Fig. 11 **A** Cross-sectional SEM images of model samples prepared with different ratios of porcine blood to lime water after freeze-drying; **B** SEM image and water contact angle for the mixture of porcine blood and sodium hydroxide after freeze-drying; **C** Intermolecular forces existing in porcine blood fibrin proteins

to 11 with sodium hydroxide, as shown in Fig. 11B. This sample exhibited a uniformly and densely distributed pore structure, which was completely different from the lamellar pore structure of the porcine blood shown in Fig. 11A (PB). This indicated that the interaggregates of fibrin were significantly weakened at high basicity, proving that alkali indeed disaggregated the fibrin assemblies.

Based on the literature [17–19, 71], sodium chloride, urea, and β -mercaptoethanol were used to detect ionic bonds, hydrogen bonds, hydrophobic interactions, and disulfide bonds in the proteins present in porcine blood. The results are shown in Fig. 11C and indicated that ionic bonds played major roles in both the intermolecular and intramolecular interactions in porcine blood. This was followed by hydrophobic interactions as well as hydrogen bonds and disulfide bonds. Table 2 shows that sodium hydroxide had a significant effect on the viscosity of the porcine blood, highlighting the important role of ionic interactions in maintaining the native conformations of the porcine blood fibrin proteins. Despite the importance of hydrophobic interactions in preserving the fibrin conformations, this role was easily weakened by changes in the conformation of fibrillin [44].

In the mixture of porcine blood and lime water, in addition to the intermolecular and intramolecular interactions shown in Fig. 11C, there was also coordination

bonding between calcium ions and the negatively charged carboxyl groups of fibrin. As mentioned earlier, these coordination bonds between Ca^{2+} and carboxyl groups were responsible for chemical crosslinking [8, 29]. However, when a smaller amount of lime water was introduced into a sample, such as in PB, $\text{PBG}_{0.03}$, and $\text{PBG}_{0.04}$, these coordination bonds alone were not sufficient to affect the self-assembled structures of the protofibrils. Therefore, some furcate lamellar structures still existed in these samples (Fig. 11A). On the other hand, when enough lime water was added to the samples, the coordination bonds between Ca^{2+} and the carboxyl groups were sufficient to alter both the microcosmic pore structure and the macroscopic gelatinous state [21]. In addition to the carbon-terminal carboxyl groups on fibrin, acidic amino acid residues on fibrin chains also coordinated with the calcium ions [74]. The self-assembled structures of porcine blood fibrils in different solutions, including water, sodium hydroxide solution, and lime water, are shown in Fig. 12.

Load–displacement of the porcine blood hydrogels

The load–displacement curves and breaking stresses of the model samples prepared with different ratios of porcine blood and lime water are shown in Fig. 13A. For all samples with displacements less than 0.75 mm, the load

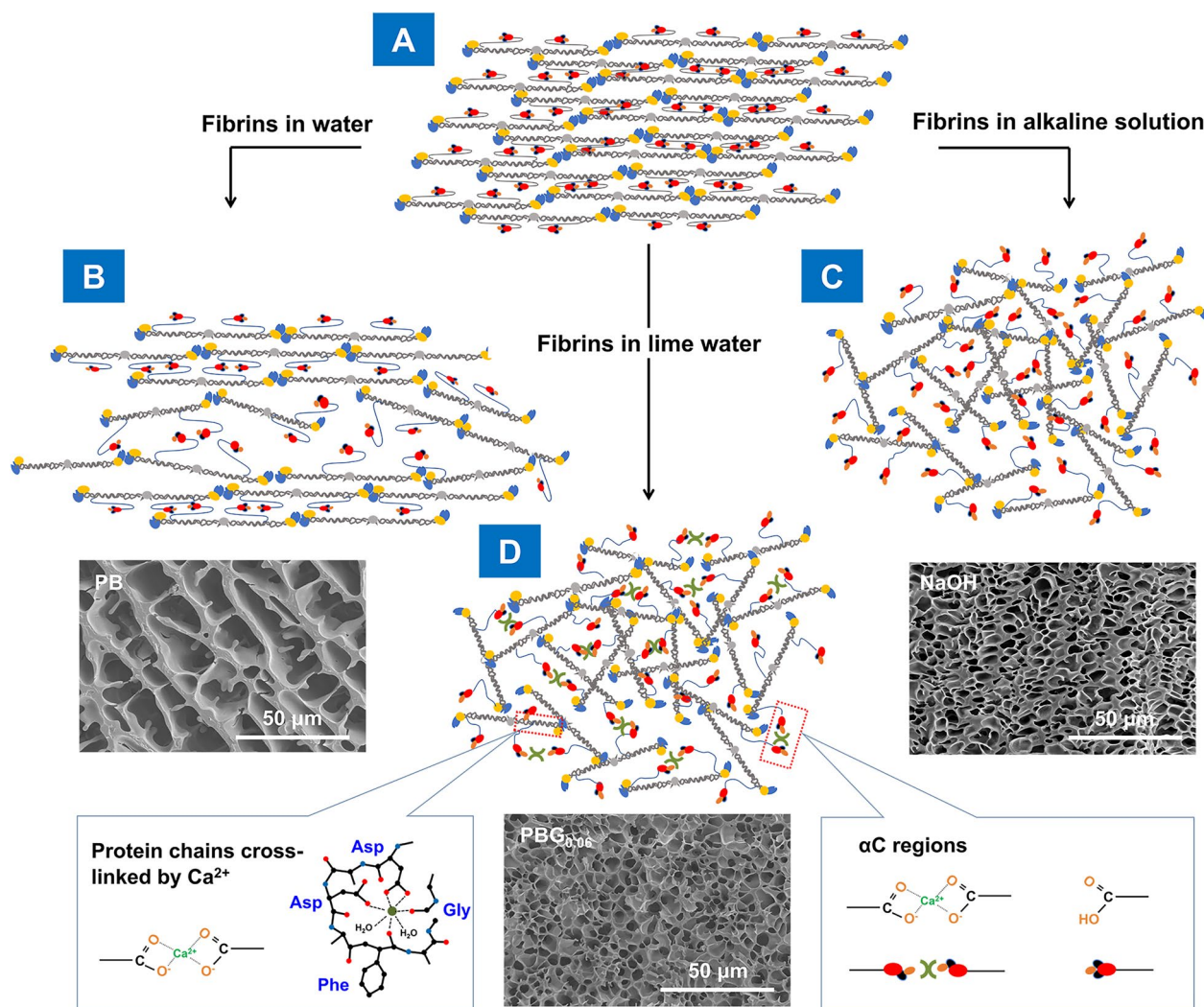


Fig. 12 Schematic representation of the self-assembled structures of porcine blood fibrin in water (B), sodium hydroxide solution (C) and lime water (D). Note: A Protofibrils self-assembled formed dimers and trimers or large oligomers, which combined the aggregation through lateral interactions between the two carbon termini and further aggregate to form a fibrous network with weak longitudinal interactions

strength changed slightly with increasing displacement, suggesting that all samples experienced similar structural changes during this process. This feature was attributed to the longitudinal linkages in fibrin self-assembled bodies, which occurred mainly through so-called “knob-hole interactions”. These interactions were weak and occurred first upon forced stretching of fibrin oligomers, and they were essential for elongation of the fibrin strands [71]. However, when a PB sample was used as a reference, the added lime water resulted in two completely opposite results: a decrease or an increase in the breaking stress. Compared with those of PB, for the PBG_{0.03} and PBG_{0.04} samples in which a small amount of lime water was introduced, the breaking stresses decreased, while for the PBG_{0.05}, PBG_{0.06}, and PBG_{0.07} samples in which large

amounts of lime water were added, the breaking stresses increased. This may be related to two effects of lime water on porcine blood fibrin proteins. First, deprotonation of the carboxyl groups of the proteins by lime water weakened the hydrogen bonds between fibrin proteins. Second, calcium ions from the lime water coordinated with the deprotonated carboxyl groups on the protein chains, leading to enhanced cross-linking. When only a small amount of lime water was introduced, the weakened hydrogen bonds were dominant, whereas when a large amount of lime water was added, enhanced cross-linking was dominant.

Complete deprotonation of the carboxyl groups on fibrin with excess sodium hydroxide resulted in a significant reduction in the blood viscosity (Table 2, PB_{A4},

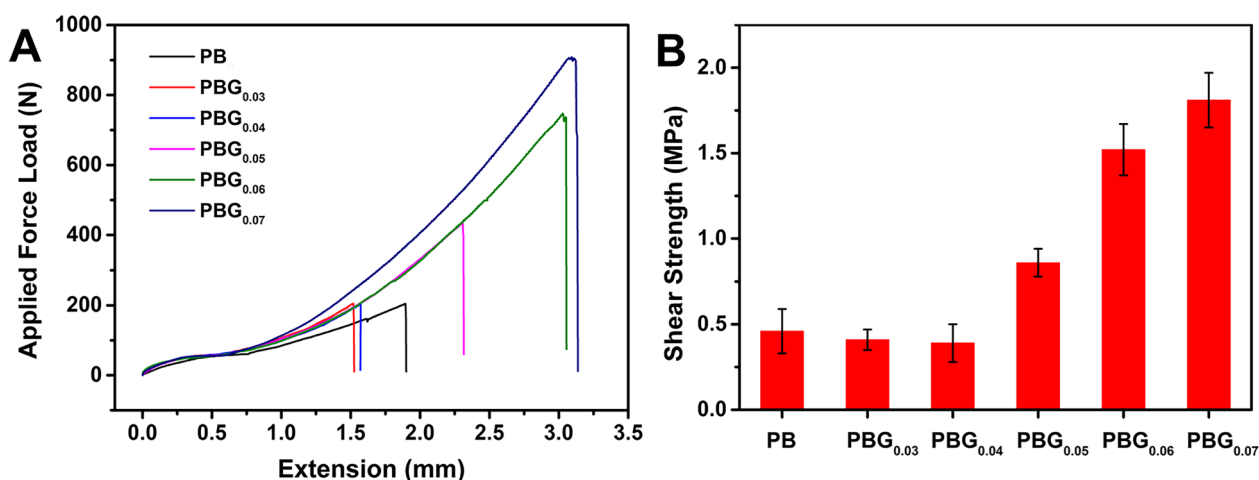


Fig. 13 Load–displacement curves (A) and breaking stresses (B) of the samples prepared with different ratios of porcine blood to lime water

pH=13). However, at the same pH (Table 2, PB_{Ca-A7}, pH=13), porcine blood was gelled by the Ca²⁺ ions, proving the effectiveness of Ca²⁺ cross-linking in increasing the mechanical strength of porcine blood. This effect was confirmed by the finding that increasing amounts of lime water used to prepare porcine blood hydrogels led to greater breaking stresses (Fig. 13A and B). Additionally, Fig. 11A shows that the addition more lime water increased the pore density of the porcine blood hydrogel, which was consistent with the above conclusion. It is worth noting that despite weakening of mechanical properties caused by alkalinity-induced deprotonation, the porcine blood hydrogels exhibit stronger mechanical properties when large amounts of lime water were introduced, primarily due to calcium ion coordination. We expect this strong bonding of porcine blood hydrogels will increase the mechanical strengths of the composite interactions with tung oil.

The fracture surface morphology provides valuable information for determining the fracture mechanism. SEM images of the fracture surfaces of the model samples prepared with different ratios of porcine blood to lime water are shown in Fig. 14. As the amount of lime water was increased, the roughnesses of the fracture surfaces of the prepared samples increased. It was observed that samples with rough fracture surfaces exhibited higher fracture resistance [74], indicating an enhanced ability to resist fractures when the lime water was introduced. This conclusion was supported by examining the details of the fracture interface morphology depicted in Fig. 14. For the PB sample, most of the smooth structural features were found on the fracture surface, but there were also small spots and fine filaments caused by slight deformations, reflecting susceptibility for fractures.

For PBG_{0.03}, cleavage fractures in a river pattern dominated the micromorphology, representing typical brittle characteristics. For PBG_{0.04} and PBG_{0.05}, their fracture surfaces displayed river-like patterns along with microdeformation traces, suggesting a combination of brittle and slightly tough fractures. In contrast, both PBG_{0.06} and PBG_{0.07} exhibited mixed morphological characteristics on their fracture surfaces; low roughness plane structures combined with highly dimpled structures were observed. This indicated that both samples had strong mechanical properties. Notably, due to the more pronounced dimple structures present on the PBG_{0.07} fractured surface compared to the other samples, it was concluded that PBG_{0.07} had even stronger mechanical properties. The conclusion drawn from the fractal surface morphologies was consistent with the changes in mechanical properties. The cross-linked structure formed by coordination between calcium ions and carboxyl groups on the fibrin chains was the key to improving the mechanical properties of the pig blood hydrogels.

Conclusions

Although the performance of porcine blood-lime mortar has been widely investigated, the mechanism of porcine blood hydrogel formation, which is the main raw material in this mortar, remains poorly understood. Based on the present investigation, the following conclusions were drawn.

- (1) Gelation of the porcine blood required an appropriate amount of lime water. Adequate alkalinity deprotonated sufficient carboxyl groups on the fibrin chains and the appropriate amount of Ca²⁺

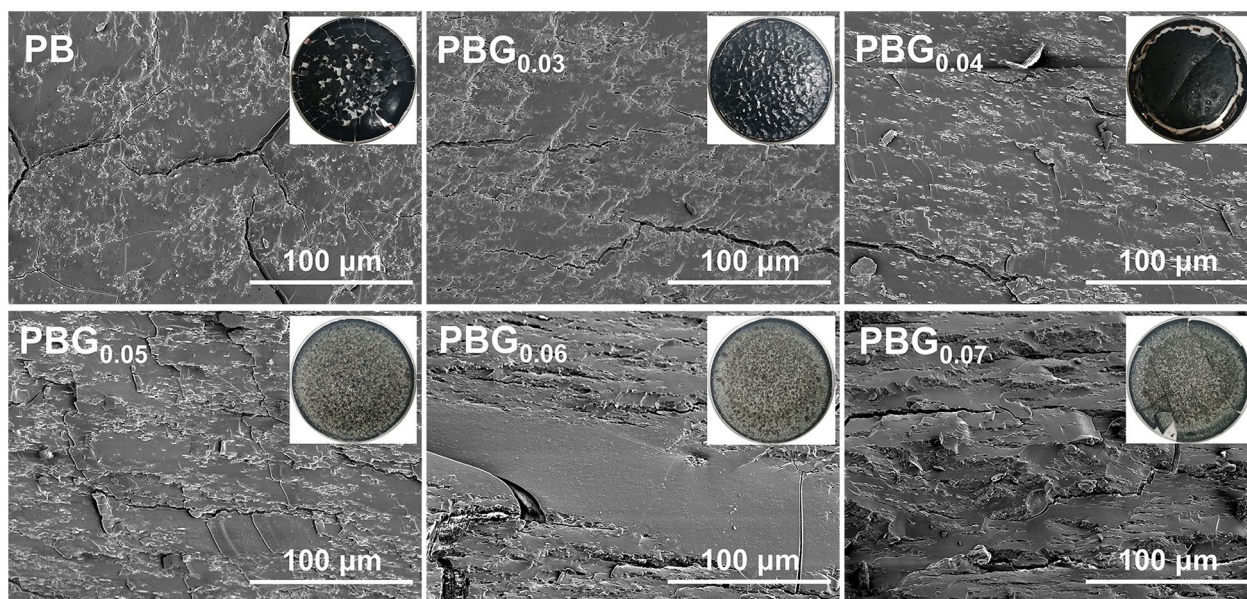


Fig. 14 Cross-sectional SEM images of porcine blood hydrogels after natural drying. PB and PBG refer to porcine blood and model samples of porcine blood mixed with lime water at different ratios

ions coordinated with the deprotonated carboxyl groups to form enough cross-links to support the network structure of the porcine blood hydrogels. In the absence of calcium ions, excess alkali increased the repulsion between the negatively charged carboxylate groups, which decreased interactions between the fibrin proteins.

- (2) Both deprotonation of the carboxyl groups on the fibrin chains and coordination of Ca^{2+} ions significantly affected the fiber protein conformation. Conformational changes caused by these factors resulted in alternative aggregated states of the fibrin proteins.
- (3) In the presence of lime water, the thiol groups on the fibrin protein chains were oxidized to form disulfide bonds or sulfates, and these reactions may be related to catalytic oxidation of the heme in blood.
- (4) Porcine blood at the microscale exhibited intermolecular laminar aggregates accompanied by weak interlaminar crosslinking. This pattern was equivalent to self-assembly, in which native fibrin swelled anisotropically.
- (5) Laminar aggregates of fibrin were disintegrated by deprotonation of the carboxyl groups on the fibrin chains and coordination cross-linking with Ca^{2+} ions to form homogeneous 3D porous structures. As the concentration of Ca^{2+} in the porcine blood increased, the hydrogel pore density also increased, resulting in enhanced mechanical properties.

The durability of ancient building mortar was determined by the materials. Porcine blood hydrogels provided strong adhesion, and hydrophobic surfaces that enabled better mixing with tung oil, thereby enhancing the adhesion and water resistance of the mortar. We hope that this work will deepen our understanding of this traditional material and provide useful information for conservation and restoration of historic buildings.

Abbreviations

PB	Porcine Blood
PBG	Porcine Blood hydrogel
FTIR	Fourier Transform Infrared Spectroscopy
XRD	X-ray diffraction
XPS	X-ray photoelectron

Supplementary Information

The online version contains supplementary material available at <https://doi.org/10.1186/s40494-024-01191-8>.

Additional file 1: Figure S1. Determination of bonding shearing strength.

Acknowledgements

The author thanks the National Natural Science Foundation (No. 21773150) for its project support and the other members of the research team for their scientific research assistance.

Author contributions

CC conducted experiments and wrote a manuscript; YZ analyzed the results; JZ and GT drew figures and tables; LZ and WL designed experiments and revised the manuscript; DH. Conceptualize and supervise. All authors have read and agreed to the published version of the manuscript.

Funding

This study was funded by the National Natural Science Foundation of China (No. 21773150) and the Shaanxi Youth Science Foundation (Approval No. 2023-JC-QN-0072).

Availability of data and materials

The datasets used and/or analysis during the current study are available from the corresponding author on reasonable request.

Declarations

Competing interests

The authors declare that they have no competing financial interests.

Received: 8 December 2023 Accepted: 23 February 2024

Published online: 01 March 2024

References

1. IRCMC. Restoration technology of traditional Chinese architecture. Beijing: Press of Chinese Architectural Industry; 1998.
2. Gang Z. Techniques and methods of the preservation and restoration of the decorative paintwork of the ancient architecture. *Relics Museology*. 2015. <https://doi.org/10.3969/j.issn.1000-7954.2015.04.015>.
3. Zhang K, Rampazzi L, Riccardi MP, Sansonetti A, Grimoldi A. Mortar mixes with oxblood: historical background, model sample recipes and properties. 2018. *Adv Geosci*. <https://doi.org/10.5194/adgeo-45-19-2018>.
4. Zhang K, Zhang BJ, Fang SQ. The application history and scientific nature of blood-based materials in traditional Chinese mortar. *Sci Conserv Archaeol*. 2013;25:94–102. <https://doi.org/10.16334/j.cnki.cn31-1652/k.2013.02.006>.
5. Zhang BJ, Fang SQ, Li JJ. Chinese traditional composite mortar. Beijing: China Building Materials Press; 2020.
6. Rao H, Li B, Yang Y, Ma Q, Wang C. Proteomic identification of organic additives in the mortars of ancient Chinese wooden buildings. *Anal Methods*. 2015;7:143–9. <https://doi.org/10.1039/c4ay01766h>.
7. Hu D, Li Y, Li J, Li H, Hu X, Ma T. Some scientific information in technical process of colored drawing on Chinese ancient building. *Relics Museology*. 2009. <https://doi.org/10.1016/j.vibspec.2021.103291>.
8. Fang S, Zhang K, Zhang H, Zhang B. A study of traditional blood lime mortar for restoration of ancient buildings. *Cem Concr Res*. 2015;76:232–41. <https://doi.org/10.1016/j.cemconres.2015.06.006>.
9. Miklin-Kniefacz S, Pitthard V, Parson W, Berger C, Stanek S, Griesser M, et al. Searching for blood in Chinese lacquerware: zhū xiě huī 豬血灰. *Stud Conserv*. 2016;61:45–51. <https://doi.org/10.1080/00393630.2016.1227039>.
10. Dinç-Şengönlü B, Yüzer N, Boylu S, Erdil K, Gündendede YA. Utilization of waste animal blood as an additive in hydraulic lime-based mortars. *Constr Build Mater*. 2023;400: 132909. <https://doi.org/10.1016/j.conbuildmat.2023.132909>.
11. Lin H, Gunasekaran S. Cow blood adhesive: characterization of physico-chemical and adhesion properties. *Int J Adhes Adhes*. 2010;30:139–44. <https://doi.org/10.1016/j.jadhadh.2009.10.003>.
12. Zhao P, Xie DQ, Li GY, Zhang YS. An experimental study of pig blood-lime mortar used on ancient architecture in China. *Adv Mater Res*. 2014;997:496–9. <https://doi.org/10.4028/www.scientific.net/AMR.997.496>.
13. Schellmann NC. Animal glues: a review of their key properties relevant to conservation. *Stud Conserv*. 2007;52:55–66. <https://doi.org/10.1179/sic.2007.52.Supplement-1.55>.
14. Fevzioglu M, Ozturk OK, Hamaker BR, Campanella OH. Quantitative approach to study secondary structure of proteins by FT-IR spectroscopy, using a model wheat gluten system. *Int J Biol Macromol*. 2020;164:2753–60. <https://doi.org/10.1016/j.ijbiomac.2020.07.299>.
15. Ghimire H, Venkataramani M, Bian Z, Liu Y, Perera AGU. ATR-FTIR spectral discrimination between normal and tumorous mouse models of lymphoma and melanoma from serum samples. *Sci Rep*. 2017;7:16993. <https://doi.org/10.1038/s41598-017-17027-4>.
16. Zubavichus Y, Zharnikov M, Shaporenko A, Fuchs O, Weinhardt L, Heske C, et al. Soft x-ray induced decomposition of phenylalanine and tyrosine: a comparative study. *J Phys Chem A*. 2004;108:4557–65. <https://doi.org/10.1021/jp049376f>.
17. Lowry O, Rosebrough N, Farr AL, Randall R. Protein measurement with the folin phenol reagent. *J Biol Chem*. 1951;193:265–75. [https://doi.org/10.1016/S0021-9258\(19\)52451-6](https://doi.org/10.1016/S0021-9258(19)52451-6).
18. Pérez-Mateos M, Lourenco H, Montero P, Borderías AJ. Rheological and biochemical characteristics of high-pressure and heat induced gels from blue whiting (*Micromesistius poutassou*) muscle proteins. *J Agric Food Chem*. 1997;45:44–9. <https://doi.org/10.1021/JF960185M>.
19. Tan F-J, Lai K-M, Hsu K-C. A comparative study on physical properties and chemical interactions of gels from tilapia meat pastes induced by heat and pressure. *J Texture Stud*. 2010;41:153–70. <https://doi.org/10.1111/j.1745-4603.2010.00219.x>.
20. Zhao Y, Chen Z, Li J, Xu M, Shao Y, Tu Y. Formation mechanism of ovalbumin gel induced by alkali. *Food Hydrocolloids*. 2016;61:390–8. <https://doi.org/10.1016/j.foodhyd.2016.04.041>.
21. Dominik H. Fibrillogenesis and hydrogel formation from fibrinogen induced by calcium salts. *Gels*. 2023. <https://doi.org/10.3390/gels9030175>.
22. Miller LM, Bourassa MW, Smith RJ. FTIR spectroscopic imaging of protein aggregation in living cells. *Biochim Biophys Acta*. 2013;1828:2339–46. <https://doi.org/10.1016/j.bbamem.2013.01.014>.
23. Long G, Ji Y, Pan H, Sun Z, Li Y, Qin G. Characterization of thermal denaturation structure and morphology of soy glycinin by FTIR and SEM. *Int J Food Prop*. 2015;18:763–74. <https://doi.org/10.1080/10942912.2014.908206>.
24. Lozano M, Rodríguez-Ulibarri P, Echeverría JC, Beruete M, Sorolla M, Berain MJ. Mid-infrared spectroscopy (MIR) for simultaneous determination of fat and protein content in meat of several animal species. *Food Anal Methods*. 2017;10:3462–70. <https://doi.org/10.1007/s12161-017-0879-1>.
25. Kobayashi Y, Mayer SG, Park JW. FT-IR and Raman spectroscopies determine structural changes of tilapia fish protein isolate and surimi under different comminution conditions. *Food Chem*. 2017;226:156–64. <https://doi.org/10.1016/j.foodchem.2017.01.068>.
26. Yang K, Zhou Y, Guo J, Feng X, Wang X, Wang L, et al. Low frequency magnetic field plus high pH promote the quality of pork myofibrillar protein gel: a novel study combined with low field NMR and Raman spectroscopy. *Food Chem*. 2020;326: 126896. <https://doi.org/10.1016/j.foodchem.2020.126896>.
27. Diletta A, Barbara S, Paolo M, Jacopo F, Tiziano C, Cristina V, et al. Pathological ATX3 expression induces cell perturbations in *E. coli* as revealed by biochemical and biophysical investigations. *Int J Mol Sci*. 2021. <https://doi.org/10.3390/ijms22020943>.
28. Sadat A, Joye I. Peak fitting applied to fourier transform infrared and raman spectroscopic analysis of proteins. *Appl Sci*. 2020;10:5918. <https://doi.org/10.3390/app10175918>.
29. Yongsawatdigul J, Carvajal-Rondanelli P, Lanier T. Surimi gelation chemistry. *Surimi Surimi Seafood*. 2005;2:435–89. <https://doi.org/10.1201/9781420028041.ch10>.
30. Lykina A, Artemyev D, Bratchenko I, Khristoforova Y, Myakinin O, Kuzmina T, et al. Raman spectra analysis of human blood protein fractions using the projection on latent structures method. *CEUR Workshop Proc*. 2017. <https://doi.org/10.18287/1613-0073-2017-1900-64-68>.
31. Premasiri WR, Lee JC, Ziegler LD. Surface-enhanced Raman scattering of whole human blood, blood plasma, and red blood cells: cellular processes and bioanalytical sensing. *J Phys Chem B*. 2012;116:9376–86. <https://doi.org/10.1021/jp304932g>.
32. Kuhar N, Sil S, Umapathy S. Potential of Raman spectroscopic techniques to study proteins. *Spectrochim Acta Part A Mol Biomol Spectrosc*. 2021;258: 119712. <https://doi.org/10.1016/j.saa.2021.119712>.
33. Widjaja E, Garland M. Detection of bio-constituents in complex biological tissue using Raman microscopy. *Appl Human Nail Clipp Talanta*. 2010;80:1665–71. <https://doi.org/10.1016/j.talanta.2009.10.006>.
34. Nagano N, Ota M, Nishikawa K. Strong hydrophobic nature of cysteine residues in proteins. *FEBS Lett*. 1999;458:69–71. [https://doi.org/10.1016/S0014-5793\(99\)01122-9](https://doi.org/10.1016/S0014-5793(99)01122-9).
35. Catalano C, Al Mughram MH, Guo Y, Kellogg GE. 3D interaction homology: Hydrophobic interaction environments of serine and cysteine are strikingly different and their roles adapt in membrane proteins. *Curr Res Struct Biol*. 2021;3:239–56. <https://doi.org/10.1016/j.crstbi.2021.09.002>.

36. Neugebauer U, Clement JH, Bocklitz T, Krafft C, Popp J. Identification and differentiation of single cells from peripheral blood by Raman spectroscopic imaging. *J Biophotonics*. 2010;3:579–87. <https://doi.org/10.1002/jbio.201000020>.
37. Luo J, Luo J, Li X, Li K, Gao Q, Li J. Toughening improvement to a soybean meal-based bioadhesive using an interpenetrating acrylic emulsion network. *J Mater Sci*. 2016;51:9330–41. <https://doi.org/10.1007/s10853-016-0180-5>.
38. Hazrati Z, Madadlou A. Gelation by bioactives: Characteristics of the cold-set whey protein gels made using gallic acid. *Int Dairy J*. 2021;117: 104952. <https://doi.org/10.1016/j.idairyj.2020.104952>.
39. Chang J, Yang X, Li J, Fu Q, Zhou J, Zhao J, et al. Improvement of physicochemical and gel properties of chlorogenic acid-modified oxidized myofibrillar proteins by transglutaminase. *LWT*. 2023;178: 114582. <https://doi.org/10.1016/j.lwt.2023.114582>.
40. Goetze J, Yarulina I, Gascon J, Kapteijn F, Weckhuysen BM. Revealing lattice expansion of small-pore zeolite catalysts during the methanol-to-olefins process using combined operando X-ray diffraction and UV–vis spectroscopy. *ACS Catal*. 2018;8:2060–70. <https://doi.org/10.1021/acscatal.7b04129>.
41. Yang J, Zhu B, Dou J, Li X, Tian T, Tong X, et al. Structural characterization of soy protein hydrolysates and their transglutaminase-induced gelation properties. *LWT*. 2023;179: 114668. <https://doi.org/10.1016/j.lwt.2023.114668>.
42. Barazzouk S, Daneault C. Amino acid and peptide immobilization on oxidized nanocellulose: spectroscopic characterization. *Nanomaterials*. 2012;2:187–205. <https://doi.org/10.3390/nano2020187>.
43. Artemenko A, Shchukarev A, Štenclová P, Wågberg T, Segervald J, Jia X, et al. Reference XPS spectra of amino acids. *IOP Conf Ser Mater Sci Eng*. 2021;1050:12001. <https://doi.org/10.1088/1757-899X/1050/1/012001>.
44. Cottrell BA, Strong DD, Watt KW, Doolittle RF. Amino acid sequence studies on the alpha chain of human fibrinogen. Exact location of cross-linking acceptor sites. *Biochemistry*. 1979;18:5405–10. <https://doi.org/10.1021/bi00591a023>.
45. Podolnikova NP, Yakovlev S, Yakubenko VP, Wang X, Gorkun OV, Ugarova TP. The interaction of integrin $\alpha_{IIb}\beta_3$ with Fibrin occurs through multiple binding sites in the α_{IIb} β -propeller domain. *J Biol Chem*. 2014;289:2371–83. <https://doi.org/10.1074/jbc.M113.518126>.
46. Zhao X, Zhu H, Zhang B, Chen J, Ao Q, Wang X. XRD, SEM, and XPS analysis of soybean protein powders obtained through extraction involving reverse micelles. *J Am Oil Chem Soc*. 2015;92:975–83. <https://doi.org/10.1007/s11746-015-2657-9>.
47. Huang J, Shen J, Li S, Cai J, Wang S, Lu Y, et al. TiO₂ nanotube arrays decorated with Au and Bi₂S₃ nanoparticles for efficient Fe³⁺ ions detection and dye photocatalytic degradation. *J Mater Sci Technol*. 2020;39:28–38. <https://doi.org/10.1016/j.jmst.2019.04.043>.
48. Bronze-Uhle ES, Dias LFG, Trino LD, Matos AA, de Oliveira RC, Lisboa-Filho PN. Physicochemical characterization of albumin immobilized on different TiO₂ surfaces for use in implant materials. *Colloids Surf A*. 2019;564:39–50. <https://doi.org/10.1016/j.colsurfa.2018.12.028>.
49. Senkevich JJ, Mitchell CJ, Yang GR, Lu TM. Surface chemistry of mercaptan and growth of pyridine short-chain alkoxy silane molecular layers. *Langmuir*. 2002;18:1587–94. <https://doi.org/10.1021/la010970f>.
50. Butera D, Hogg PJ. Fibrinogen function achieved through multiple covalent states. *Nat Commun*. 2020;11:5468. <https://doi.org/10.1038/s41467-020-19295-7>.
51. Mishanina TV, Libiad M, Banerjee R. Biogenesis of reactive sulfur species for signaling by hydrogen sulfide oxidation pathways. *Nat Chem Biol*. 2015;11:457–64. <https://doi.org/10.1038/nchembio.1834>.
52. Kehm R, Baldensperger T, Rauppach J, Höhn A. Protein oxidation—formation mechanisms, detection and relevance as biomarkers in human diseases. *Redox Biol*. 2021;42: 101901. <https://doi.org/10.1016/j.redox.2021.101901>.
53. Jani KK, Barad DV, Raval PY, Nehra M, Vasoya NH, Jakhar N, et al. Ca²⁺ - substitution effect on the electronic structure of CaCu₃Ti₄O₁₂ studied by electron spectroscopy for chemical analysis. *Ceram Int*. 2021;47:5542–8. <https://doi.org/10.1016/j.ceramint.2020.10.138>.
54. Liu Q, Li J, Zhou Z, Xie J, Lee JY. Hydrophilic mineral coating of membrane substrate for reducing internal concentration polarization (ICP) in forward osmosis. *Sci Rep*. 2016;6:19593. <https://doi.org/10.1038/srep19593>.
55. Mukherjee M, Dey A. Catalytic C–H bond oxidation using dioxygen by analogues of heme superoxide. *Inorg Chem*. 2020;59:7415–25. <https://doi.org/10.1021/acs.inorgchem.9b03767>.
56. Gowder SM, Chatterjee J, Chaudhuri T, Paul K. Prediction and analysis of surface hydrophobic residues in tertiary structure of proteins. *Sci World J*. 2014. <https://doi.org/10.1155/2014/971258>.
57. Marriott G, Kirk WR, Johnsson N, Weber K. Absorption and fluorescence spectroscopic studies of the calcium-dependent lipid binding protein P36: the annexin repeat as the calcium binding site. *Biochemistry*. 1990;29:7004–11. <https://doi.org/10.1021/bi00482a008>.
58. Vivian JT, Callis PR. Mechanisms of tryptophan fluorescence shifts in proteins. *Biophys J*. 2001;80:2093–109. [https://doi.org/10.1016/S0006-3495\(01\)76183-8](https://doi.org/10.1016/S0006-3495(01)76183-8).
59. Li R, Dhankhar D, Chen J, Cesario T, Rentzepis P. A tryptophan synchronous and normal fluorescence study on bacteria inactivation mechanism. *Proc Natl Acad Sci*. 2019;116:201909722. <https://doi.org/10.1073/pnas.1909722116>.
60. Gonçalves S, Santos NC, Martins-Silva J, Saldanha C. Fibrinogen- β -Estradiol binding studied by fluorescence spectroscopy: denaturation and pH Effects. *J Fluoresc*. 2006;16:207–13. <https://doi.org/10.1007/s10895-005-0051-y>.
61. Renard D, Lefebvre J, Griffin MCA, Griffin WG. Effects of pH and salt environment on the association of β -lactoglobulin revealed by intrinsic fluorescence studies. *Int J Biol Macromol*. 1998;22:41–9. [https://doi.org/10.1016/S0141-8130\(97\)00086-X](https://doi.org/10.1016/S0141-8130(97)00086-X).
62. Bhagat V, Becker ML. Degradable adhesives for surgery and tissue engineering. *Biomacromol*. 2017;18:3009–39. <https://doi.org/10.1021/acs.biomac.7b00969>.
63. Wang L, Tiu C, Liu TJ. Effects of nonionic surfactant and associative thickener on the rheology of polyacrylamide in aqueous glycerol solutions. *Colloid Polym Sci*. 1996;274:138–44. <https://doi.org/10.1007/BF00663445>.
64. Saluja A, Kalonia DS. Nature and consequences of protein–protein interactions in high protein concentration solutions. *Int J Pharm*. 2008;358:1–15. <https://doi.org/10.1016/j.ijpharm.2008.03.041>.
65. Hospodiuk M, Dey M, Sosnoski D, Ozbolat IT. The bioink: a comprehensive review on bioprintable materials. *Biotechnol Adv*. 2017;35:217–39. <https://doi.org/10.1016/j.biotechadv.2016.12.006>.
66. Guo J, Zhou Y, Yang K, Yin X, Ma J, Li Z, et al. Effect of low-frequency magnetic field on the gel properties of pork myofibrillar proteins. *Food Chem*. 2019;274:775–81. <https://doi.org/10.1016/j.foodchem.2018.09.028>.
67. del Hoyo P, Rendueles M, Díaz M. Decolorized porcine globin gels produced by heat-induced gelation. Physical and rheological characterization. *J Food Eng*. 2012;113:245–53. <https://doi.org/10.1016/j.jfoodeng.2012.05.042>.
68. Guocan Y, Xuzhou Y, Chengyou H, Feihe H. Characterization of supramolecular gels. *Chem Soc Rev*. 2013;42:6697–722. <https://doi.org/10.1039/c3cs60080g>.
69. Piechocka IK, Bacabac RG, Potters M, MacKintosh FC, Koenderink GH. Structural hierarchy governs fibrin gel mechanics. *Biophys J*. 2010;98:2281–9. <https://doi.org/10.1016/j.bpj.2010.01.040>.
70. Wj W, Lr I. Mechanisms of fibrin polymerization and clinical implications. *Blood*. 2013. <https://doi.org/10.1182/blood-2012-09-306639>.
71. Kim W-J, Kang JG, Kim D-W. Blood clot-inspired viscoelastic fibrin gel: new aqueous binder for silicon anodes in lithium ion batteries. *Energy Storage Mater*. 2022;45:730–40. <https://doi.org/10.1016/j.ensm.2021.12.024>.
72. Gonzalez X. Influence of the nature of fibrinogen on the structure and mechanics of fibrin clots. Grenoble: Université Grenoble Alpes; 2016.
73. Phillips LG, Whitehead DM, Kinsella JE. Structure-function properties of food proteins. *Protein Gelation*. 1994. <https://doi.org/10.1016/b978-0-12-554360-6.50014-0>.
74. Huang S, Lin J, Wang N, Guo B, Jiang F, Wen Q, et al. Fracture behavior of single-crystal sapphire in different crystal orientations. *Crystals*. 2021. <https://doi.org/10.3390/cryst11080930>.

Publisher's Note

Springer Nature remains neutral with regard to jurisdictional claims in published maps and institutional affiliations.